Investigations of a Circulation Control Airfoil Flowfield using an Advanced Laser Velocimeter

Charles J. Novak and Kenneth C. Cornelius
Lockheed-Georgia Company, Marietta, Ga. 30063

ABSTRACT

The flowfield of a Circulation Control Airfoil has been examined in detail through the use of a specially designed wind tunnel model and test program. Surface pressures on the model were obtained and the velocity field was surveyed in the trailing edge region of the model airfoil using the non-intrusive Laser Velocimetry (LV) technique. In this region mean flow and turbulence measurements indicate that, while the flowfield is similar to other wall-bounded jet flows, the external freestream plays an important role in the overall mixing and structure of the wall bounded flow. Finally, the turbulence measurements have been used to compute eddy viscosities for the purpose of aiding Computational Fluid Dynamics (CFD) model development

NOMENCLATURE

b	airfoil model span (0.61 meters)
c	airfoil model chord length (0.38 meters)
C_L	lift coefficient
Cp	surface pressure coefficient
C_μ	jet momentum coefficient
C_1	curvature constant (= 25.0)
Dp	diameter of seeding particle
h	jet slot height
K	flowfield stability parameter
$\dot{m}j$	jet massflow
Q	wind tunnel dynamic pressure
r	radius of trailing edge
Re	Reynolds number based on airfoil chord length
S	airfoil model surface area
St	Stokes number = $\frac{1}{18}\ \frac{\rho_p}{\rho_a}\ \frac{U_j D_p}{\nu}\ \frac{Dp}{r}$
U,V	mean velocities in the tangential and normal directions respectively
U_e	velocity at the edge of the mixing region ($\overline{uv}$=0.0)
U_m	maximum tangential velocity
ΔU_m	defect velocity (=U_m-U_e)
U_j	mean jet velocity expanded isentropically to freestream static pressure
U_∞	wind tunnel freestream velocity
u_τ	friction velocity
$\bar{u}'$,$\bar{v}'$	time averaged turbulent velocities in tangential and normal directions respectively
$\overline{uv}$	time averaged turbulent shear stress
x	distance along the airfoil chordline
y	normal distance above airfoil surface

$y_{1/2}$	position above surface where $U=(U_m+U_e)/2$
y_m	position of Um above surface
y+	position above surface in Law of the Wall coordinates
α	airfoil angle of attack
ε	kinematic eddy viscosity
θ	angle defining coordinate on circular trailing edge on model
ρ_p	density of seeding particle
ρ_a	density of air
ν	kinematic viscosity of air

INTRODUCTION

Modern aircraft, either for military or civilian use, are resorting to powered lift as a viable means of meeting short field requirements. One method of increasing lift is the circulation control wing (CCW). In this configuration, as seen in figure 1, a small planar jet is issued from the cylindrical trailing edge of the wing in an effort to draw the aft stagnation point under and forward of the trailing edge. Hence, net circulation is dramatically increased without resorting to a complex mechanical flap system.

This behavior arises from the characteristics of wall jets on curved surfaces, an observation dating back to 1800 when Young (1800) first described the phenomena. However, much more attention was given to Coanda in 1910 who attempted to exploit the curved wall jet. More recent interest has arisen in applying the phenomenon to CCW systems and previous examples of investigations into CCW configurations are well described in papers by Englar (1973) and Wood (1985) in which performance considerations are emphasized. Additional work includes papers by Kind & Maull (1968) and Wilson & Goldstein (1976), where the jet turning characteristics are of greatest interest.

The purpose of the experimental investigation described in this paper is to provide a definitive set of mean velocity and turbulence measurements in the aft stagnation region of a CCW wind tunnel model. A non-intrusive, 2-D Laser Velocimeter (LV) was utilized in all velocity measurements and additionally, a complete set of airfoil surface pressure data was obtained on the CCW configuration.

These data provide a valuable description of the details of the flowfield and its turbulence characteristics and are suitable for validation and comparisons with computational analyses.

EXPERIMENTAL PROCEDURE

Model Description

In an effort to satisfy both circulation control airfoil performance criteria as well as to maintain good spatial resolution with the LV in high gradient regions, a model was specially designed for use in the Lockheed-Georgia Low Turbulence Wind Tunnel (0.61x 0.92 m. and 0.03% $\bar{u}'/U_\infty$). The model is shown in figure 2 and is constructed of aluminum. It has a 0.38 m. cord with leading edge coordinates of a modern supercritical section. The symmetric mid-section and 0.051 m. diameter circulation control aft section

are blended in such a manner so as to eliminate surface discontinuities. Note that the ratio of turning radius to chord length (r/c=0.067) is somewhat high and is not representative of practical flight systems. However, this enables larger slot heights to be employed which in turn improves the LV measurement resolution.

Compressed air enters the model plenum chamber from an inlet diffuser at 90 degrees to the jet exit plane. The model's internal geometry was designed so that the jet-slot exit profile and internal flow would be of high quality and free from the effects of surface discontinuities. Two internal screens are used to accommodate internal flow smoothing and an internal fillet provides a 10:1 contraction ratio between the plenum and the jet exit as shown in figure 2.

The slot geometry is arranged so that the flow exits from the plenum tangentially to the circular Coanda surface and parallel to the upper-surface boundary. Variation in slot height is accomplished with clamp bolts located at the 75% chord line yielding slot gaps of 0.064 mm. to 3.05 mm, with an upper surface slot lip trailing edge thickness of nominally 0.25 mm. This geometry, along with a hypothetical velocity profile and the nomenclature to be used in the following discussions, is shown in figure 3.

Instrumentation on the model consists of 45 static pressure ports, each 0.5 mm. in diameter, positioned along the model centerline. A total pressure probe was located within the plenum downstream of the last screen to monitor the internal flow conditions.

Laser Velocimeter Description

The 2-D LV system used to generate the data presented in this paper is shown schematically in figure 4. It utilizes an 18-watt Argon-Ion Laser operating at 3.0 watts on all color lines. The system was operated in backscatter mode at a focal length of 0.77 meters. Receiving optics consist of a 15.4 cm. diameter lens giving an optical speed of f/5 that can be positioned in a variety of off-axis locations greater than 5 degrees. Velocity components are measured at the orthogonal intersection of the dual-green (488.0 nm.) and dual-blue (514.5 nm.) beams which may be oriented arbitrarily with respect to the tunnel coordinate system. Frequency shifting of both a green and a blue beam by the use of a Bragg cell gives the system the capability of measuring reversed flows. The measurement volume at the beam intersection is nominally 0.075 mm. in diameter by 1.3 mm. in length and signals from the photomultiplier tubes are analyzed by a specially designed counter type processor.

Typical LV electronic signals consist of a carrier d.c. voltage and a Doppler burst with a period that corresponds to the time of transit of a particle through individual fringes. If the carrier d.c. voltage is removed the signal is seen to oscillate about zero voltage level. Treatment of the signal at this point is crucial to the quality of the velocity measurement and here is where major differences between the off-the-shelf and herein described system lies.

The single-cycle verification circuitry designed in-house by Whiffen (1979) assures that the period of each cycle of the incoming signal burst is equal, within a controlled error window, to the period of the cycle preceding

it and following it. The technique has several inherent advantages over the 5/8 and 4/8 schemes that are commercially used. First, it is the ultimate extension of those schemes since it effectively takes the period comparisons to their natural limit, and so provides seven tests during the signal burst instead of one. Also, the error window width is not critical. Since the most common error in a signal burst is a dropped cycle, it results in a 100% difference in a single cycle period; whereas, with a 5/8 validation, for instance, certain combinations of dropped cycles result in only a 4% difference in period and, therefore, require very narrow, highly critical, error windows which are difficult to achieve, particularly with standard circuity components over a wide bandwidth. The 4/8 validation scheme is even worse, since combinations of dropped cycles, symmetrical about the center of the burst, i.e., about the 4th count, are impossible to detect and are thus accepted as valid data. figure 5 shows the validation criteria determined by the circuity. In effect, the circuit invalidates any signal burst in which the period for two adjacent (in time) signal cycles differ by more than the window, W. For the circuits used, W is variable between 5% and 80% of the cycle period. The end result of this is a highly accurate digital representation of the particle/fringe crossing, and, superior to that of the commercially produced counterpart.

The second feature, inherent to the LV electronics system used, increases the quality of the turbulence quantities to levels comparable to other measurement techniques (i.e., hot-wire anemometry). Figure 6 shows the effect of noise on the processor detection process. It is seen that noise actually causes a jitter in the time of each zero crossing. This jitter in turn causes random changes in the period of the measurement gate which is timed by a 500 Mhz clock and sent to the computer as raw velocity data. It is readily seen that only the first and last detected zero crossing contributes to variations in the measured period. Since the zero crossing jitter is caused by a random process, the effect at each crossing is statistically independent and uncorrelated except as convoluted by the common transfer function of the mixer and bandpass filters prior to the detector. A cursory examination of these components suggested that only the bandpass filter had a time constant which could produce noise correlation within the time frame of the signal frequencies. This effect, however, was found to decay within 3 or 4 signal cycles. Therefore, a second measurement gate was generated from the same sequence of zero crossings and was displaced for different zero crossings by 4 cycles from the first gate. This gate was then in turn timed by a second 500 Mhz clock to eliminate possible correlation between digital counting processes and recorded as the second raw velocity data point.

After the electronic processing, each data word is transmitted to the host mini-computer along with a record of the acquisition time of the measurement. This information allows subsequent reconstruction of the temporal history of the flow from which spectral and correlation data may be obtained. Also, an internal trigger may be synthesized or a trigger may be provided externally to enable conditional sampling of a flowfield to reveal phase averaged structures in the flow.

Flowfield Seeding

Prior to testing, an investigation concerning the balance of centrifugal and viscous forces on a seeding particle (LV scattering media) was

undertaken. In testing of this nature, it is most important that the flowfield seeding follows the fluid streamlines. Dring and Suo (1978) studied this situation and showed theoretically that for spherical particles below a certain size range, the viscous forces (Stokes drag) balanced forces directly attributed to swirl in the flowfield. They report that a Stokes number of St= 0.016 is needed to ensure negligible centrifugal effects. For the present test this value corresponds to a one micron diameter particle of mineral oil subjected to the acceleration along the Coanda surface. Thus the use of a particle impactor was required since the seeding size distribution had to remain under 1 micron maximum. This need is clearly shown in figure 7, where an aerodynamic particle sizer was used to determine the particle distribution before impaction. Also shown is the predicted impaction range based on the design and operation curves for the particle impactor.

During the test program, model internal and external flowfield seeding was achieved with use of an engine lubrication atomizer. A bypass valve was used to divert a portion of the generated seed to the external flow in an effort to maintain a constant LV signal intensity across the shear layer. This factor becomes an important consideration when making jet measurements using the LV technique if the effects of velocity bias are to be minimized.

Test Conditions

For LV measurement purposes, the 2.54 mm. jet gap (h/r=0.1) was chosen to improve resolution in the large velocity gradient regions. However, surface pressure measurements were also conducted at h/r=0.035, or 0.89 mm. slot height. Angle of attack sweeps were conducted for each slot height and blowing coefficient and based on that information, LV test conditions were chosen as:

h/c	=	0.067
h/r	=	0.10
α	=	0.00 deg.
U_∞	=	30.50 m/sec.
U_j/U_∞	=	4.92
$Re(c)$	=	775000.
C_μ	=	$\dot{m}_j U_j / Q S = 0.255$

With these conditions established (such that tunnel floor and ceiling flows were fully attached as well as steady) LV surveys were conducted in the aft stagnation region of the CCW model. Additional LV surveys of limited scope were made under quiescent wind tunnel conditions with the same jet stagnation pressure (1192 Pa.) as the lifting case. Comparisons of the circular wall jet and the CCW result may be made directly if needed.

Individual profiles were acquired with the LV measurement volume traversed normal to the surface at the point of interest using a 1.23 x 1.23 meter traverse table with traverse range of .75 meters in all directions and positional accuracy of 0.025 mm. Several techniques were used to aid in LV data acquisition. For example, verification circuitry on the 2-D LV aided in raising the overall signal-to-noise ratio in the near-wall region where velocity information is of particular interest. In addition to the special electronics, a spatial filter was placed at the receiving optics pinhole or point of focus. With the lower transmitting laser beam parallel to the

surface and using 20 degrees off-axis backscatter, surface glare received by the photo-multiplier tubes was thus minimized. The wind tunnel, CCW model, and 2-D LV transmitting optics are shown in figure 8.

RESULTS

In the following, surface pressure measurements are used to describe the general lifting properties of the CCW configuration. Mean velocity measurements obtained using the LV are then discussed and related to the airfoil axial pressure gradient. Turbulence measurements and the derived quantities are discussed and similarities in the flowfield between this study and other wall bounded jet investigations are addressed.

Pressure Measurements

Measured surface pressures have been converted to non-dimensional coefficients of pressure and are presented as a function of their chordwise position in figure 9a for a slot gap of 2.5 mm.(h/r=0.10) and a fixed angle of attack of 0.0 degrees. The effect of varying the blowing momentum coefficient rate, $C\mu$, is also presented in the various curves. Large negative pressures are found in the aft circulation region and the forward and aft suction peaks are a strong function of the blowing coefficient $C\mu$. Similar results are seen in figure 9b, which apply to the smaller slot gap (0.86 mm. or h/r=0.034). A close comparison of figures 9a and 9b shows that, at a given momentum coefficient, higher suction values are obtained for the smaller slot gaps. This is indicative of the major role that jet velocity plays in flowfield development on the CCW model. Figure 10 contrasts the differences in surface pressure on the Coanda surface with and without wind tunnel freestream. Note the severe adverse pressure gradient imposed upon wall jet for the lifting case, whereas the static case exhibits a near zero gradient with respect to angular location on the circular trailing edge.

The effect of jet-to-freestream velocity ratio is seen more clearly when the surface pressures are integrated over the surface, yielding a section lift coefficient, C_L. Figure 11 shows the relationship of C_L with respect to momentum coefficient, $C\mu$. Note that at the smaller slot gap tested (0.86 mm. or h/r=0.034), the 7.6-degree angle of attack case shows evidence of separated flow at the higher values of the momentum coefficient. Again, as indicated in the previous pressure data, the higher lift values occur with the smaller slot gap for a given $C\mu$. This indicates that overall mixing of the jet with the external flow is driven by the ratio of their relative velocities.

Tunnel test conditions used for the LV surveys represent an attached flow case as indicated by the trend of C_L vs. $C\mu$ at 0.0 degrees angle of attack and h/r=0.10. The non-linearity in the lower jet velocities (low $C\mu$'s with the larger slot gap) with respect to lift appears to be typical of CCW performance (Englar (1973)).

Mean Flow Measurements

Figure 12 represents a composite vector plot of the LV mean flow measurements. The effect of the jet on the mean flowfield is apparent in the

large turning angles that are exhibited. The extent of jet mixing is also seen in the overall growth of the jet. Also, it can be observed that the upper surface boundary layer is fully attached for this case. If one looks closer at the region near jet detachment, as seen in figure 13, the rear stagnation point is seen to be between 130 and 140 degrees in angular location measured from the slot on the Coanda surface. This was also seen in the pressure measurements presented previously.

Similarly, the jet exit region, when magnified greatly as in figure 14, shows evidence of the finite slot lip trailing edge thickness. A small re-circulation region associated with the 0.25 mm. trailing edge thickness can be detected. Also exhibited in the data from this location are the mean jet characteristics and the significant entrainment of the external flow into the jet region.

The mean velocity data are shown in dimensional form, for different angular positions in figure 15. Here the velocities are defined as the component tangential to the surface. The spread of the wall jet is self-evident.

In comparing these data with similar data in the literature, it is necessary to define the appropriate dimensionless variables. Considering the curved wall jet region itself, there are two scales for velocity, U_∞ and U_j, and two scales for length, h and r. Because of these multiple scales, it is very difficult, in the absence of a very large volume of data, to determine the functional form of the dimensionless variables (based on these variables) that will collapse the data.

Despite this, some useful comparisons can be made if, instead, we consider the use of scales based upon the local wall jet characteristics. For example the outer mixing region of the curved jet flow will be driven by the velocity scale $\Delta U_m=U_m-U_e$ and will have a length scale $y_{1/2}-y_m$ (see figure 3). These are the length scales suggested by Launder and Rodi (1983).

In the present case, therefore, Ue must first be determined, and this is defined as that point where the Reynolds stresses become negligible. It is shown as a function of position in figure 16. The non-linear growth is evidence of the strong pressure gradients through which the wall jet must develop. Also shown are the corresponding values of $y_{1/2}$ and y_m.

When these variables are combined in the form suggested by Launder and Rodi (1983) then the data shown in figure 17 are obtained. Also shown are the data of Kind and Maull (1968) which exhibit similar behavior as the present data. Thus for the outer part of the jet flow at least, the flow is driven by the defect velocity $\Delta U_m=U_m-U_e$. In contrast, the circular wall jet uses scaling factors of U_m and $y_{1/2}$. This is seen in figure 18, where the data from quiescent conditions is seen to behave in the well known gaussian manner.

The inner region of the wall jet will not and should not be expected to display similarity in this form. For that region, in addition to the scales discussed above, there will be the viscous scales u_τ and y^+. However these could not be recorded in the present test program so that a suitable dimensionless form of the data can not be presented.

Turbulence Quantities

Emphasis was placed on the determination of accurate turbulence information in this test program, and for that reason, a total of 4096 data points were acquired at each measurement location. With the LV operated in a constant tunnel coordinate system, rotation of the velocity vectors to a model-fixed coordinate system was needed for comparison purposes from station to station. Thus at each angular position on the model, the turbulence intensity was resolved into a normal and tangential component. Similarly, the turbulent shear stress was transformed to a component tangential to the surface at the angular location on the where the measurements were obtained.

Figure 19 shows the tangential turbulence intensity component, $\bar{u}'$,in the similarity variables suggested by Wilson and Goldstein (1976) and indicates some similarity of profiles in the regions greater than $y_{1/2}$. Further, comparisons with the results for circular wall jet experiments collated in Launder and Rodi (1983) indicate that similarity exists between profiles in the outer mixing region. However, differences in the wall-bounded region exist, but this is to be expected in different configurations due to different viscous effects. As separation is approached, outer layer similarity is naturally lost, and large stresses are obtained. In all cases, peak values are obtained close to the wall and the existence of a minimum in the distribution is indicative of the two production regions: that near the wall (a boundary layer mechanism) region, and that in the outer region (a mixing layer mechanism).

The distributions in $\bar{v}'$ are shown in figure 20 and display similar trends, although collapse of the data in the outer region is decidedly poorer. The values are, however, comparable to those reported by Launder and Rodi (1983) except at separation where very large values arise.

Reynolds Stresses

An important turbulence quantity in 2-D flowfields is the turbulent shear stress $\overline{uv}$. During this experiment emphasis was placed on the determination of shear stresses, not only for understanding the physics of the flow, but also to provide information for turbulence modelling. The turbulent shear stress, $\overline{uv}$, is plotted with respect to the local surface normals in figure 21. Near the wall the stresses are negative due to the boundary layer production mechanism. In the outer region, where the gradient is of opposite sign, the stresses are positive and positive production is preserved. As the jet spreads, the extent of non-zero stress grows and the magnitudes become quite large at separation.

These trends are more clearly indicated in figure 22 which presents the same data, non-dimensionalized on the scales U_m and $y_{1/2}$. Similar trends in uv are seen in the high surface curvature results of Smits, Young, and Bradshaw (1979). The change in sign of the stress in the outer region after separation ($\theta = 135^{o}$) is to be expected in view of the change in sign of the velocity gradient of the incoming lower surface flow. Finally, figure 23 shows the effect of the bluff trailing edge of the upper surface. Here the large shear stress associated with the small recirculation region can be observed. The finite trailing edge thickness can thus play a role in the overall mixing and turbulence development.

Turbulent Eddy Viscosities

The ability of CFD methods to accurately predict performance can hinge upon an accurate turbulence model. For that reason some of the current work was motivated to explore the effect that curvature plays in the turbulent flowfield development. An early attempt was made by Prandtl (1961) in 1939 and later by Sawyer (1962) to account for the highly curved geometry. Their efforts have resulted in the following eddy viscosity formulation.

$$-\overline{uv} = \varepsilon \, dU/dy \, [\, 1-C_1 \, K]$$

where $K = U / (r+y) \, dU/dy$ and C_1 = curvature constant

Initial evaluation of this expression using the experimental data with curvature constant $C_1 = 5.0$ (after Wilson and Goldstein (1976)) yielded trends similar to those obtained for the planar wall jet geometry but with much elevated magnitudes. Varying the curvature constant upward, until reasonable agreement with the planar wall jet results was attained yielded a value of $C_1 = 25.0$. This value for C_1 being much larger than the "best fit" for Wilson and Goldstein (1976), may be accounted for by the much smaller curvature used by this experiment. Use of the large value for C_1 is further substantiated with the experimental results obtained by Wendt (1973) for an geometry consisting of the shear flow between concentric cylinders, where it was suggested that C_1 be of the of order of the value used at present.

The resulting data are shown in figure 24. It should be noted that the eddy viscosity values become undefined at $y=y_m$ due to the zero velocity gradient. However, this is confined to a small region and is not shown for clarity. At separation, large negative values are obtained as expected. Likewise, negative values are obtained near the wall before the separation.

The values that are obtained are comparable to those of the planar wall jet; however, no kind of universality is evident. The universal use of planar data in numerical simulation of these kinds of flow should therefore be undertaken with some caution.

Turbulence Modelling Considerations

Having conducted measurements in the aft stagnation region for both the lifting and static cases, direct comparisons of the turbulence quantities are possible.

As previously shown in figure 10, the wind tunnel freestream, and hence, the aft stagnation point acts as to impose a large adverse axial pressure gradient upon the developing circular wall jet. Comparably, the quiescent conditions gave rise to the near zero axial pressure gradient. The effect of this is seen in figure 25, where the turbulent shear stresses are plotted for both flow conditions tested. Note that the position of the jet centerline velocity does not coincide with the zero crossing of the turbulent shear stress for the 40 degree data sets. However, at 130 degrees, the region of countergradient flow diminishes for the lifting case and increases for the static case (as to be expected - after Wilson and Goldstein (1976) and Rodman et. al. (1986)).

Correspondingly, when comparing the eddy viscosities (as computed in a manner described previously using $C_1 = 25.$) a notable difference is seen. Shown in figure 26 are the computed values for both lifting and static cases at the 130 degree survey location. Eddy viscosities in the near wall region for the static case behave well when using the curvature correction scheme. For the lifting case, negative values are seen, indicating that additional and unaccounted effects are present.

Based on these differences, an order of magnitude analysis was performed to determine the significance of the external flow imposed pressure gradient. Experimental data at the jet centerline for the 90 degree locations (location of maximum pressure gradient) was inserted into the axial momentum equation and assessed. The results, compiled in figure 27, indicate that the pressure gradient in the axial direction is of the same order as the mean axial convection and the curvature terms. Conversly, the static flow assessment shows that the pressure gradient is secondary, and that the curvature effects play the dominant role in flow development. This directly supports the findings as previously shown in figures 24 and 25 and suggests the need for either a higher order turbulence model or a method to account for the large pressure gradient effects when using CFD methods to model such flows.

Closing Remarks

An experimental investigation has been made of the flowfield around a circulation control wing. The prime motivation for this study has been to generate a set of data against which CFD methods may be validated. The data that have been obtained consist of the following:

(1) Wing surface pressures and integrated lift coefficients,

(2) LV surveys of the mean flow in the wall jet region,

(3) Turbulence intensities and Reynolds stresses in the wall jet.

REFERENCES

Dring, R. P. and Suo, M.: Particle Trajectories in Swirling Flows. J. Energy, Vol. 2, No. 4, July-August 1978.

Englar, R. J.: Experimental Investigation of the High Velocity Coanda Wall Jet Applied to Bluff Trailing Edge Circulation Control Airfoils. NSRDC TN. AL-308.

Kind, R.J., and Maull, D.J.: An Experimental Investigation of a Low-Speed Circulation Controlled Aerofoil. Aeronautical Quarterly, Vol. XIX May 10, 1968, pp. 170-182.

Launder, B. A. and Rodi, W.: The Turbulent Wall Jet - Measurements and Modelling. Anu. Rev. Fluid Mech. 1983, 15:429-59

Prandtl, L.: Ludwig Prandtl Gesammelte Abhandlungen (W. Tollmein, H. Schlichting, and H. Georgtler, eds.) Springer 1961, p. 775.

Rodman L.C., Jarrah M.A., Wood N.J., and Roberts, L.: Turbulence Measurements in a Plane Wall Jet. AIAA Paper 86-209, 24th Aerospace Sciences Meeting, Reno NV, January 6-9, 1986

Sawyer, R. A.: Two-Dimensional Turbulent Jets with Adjacent Boundaries. PhD thesis, Cambridge Univ., 1962.

Smits, A. J., Young, S. T. B., and Bradshaw, P.: The effect of short regions of high surface curvature on turbulent boundary layers. J. Fluid Mech., 1979, vol. 94, part 2, pp 209-242.

Wendt, F.: Turbulente Stromungen Zwichen zwei rotierenden konaxialen Zylindern. Ing. Arch., Vol. 4, 1973, p. 577

Whiffen, M.C.: Periodicity Verification Circuit. Patent Application, Lockheed P-02-487, 1979

Wilson, D. J. and Goldstein, R. J.: Turbulent Wall Jets With Cylindrical Streamwise Surface Curvature. Journal of Fluids Engineering, Vol. 96, 1976, p. 550.

Wood, N., and Nielsen, J.: Circulation Control Airfoils Past, Present, Future. AIAA Paper 85-0204, January 14-17, 1985.

Young, T.: Outlines of Experiments and Inquiries Regarding Sound and Light. Lecture to the Royal Society Jan. 16, 1800 (see Jour. Roy. Aero. Soc. Vol. 61, 1957, p. 157.

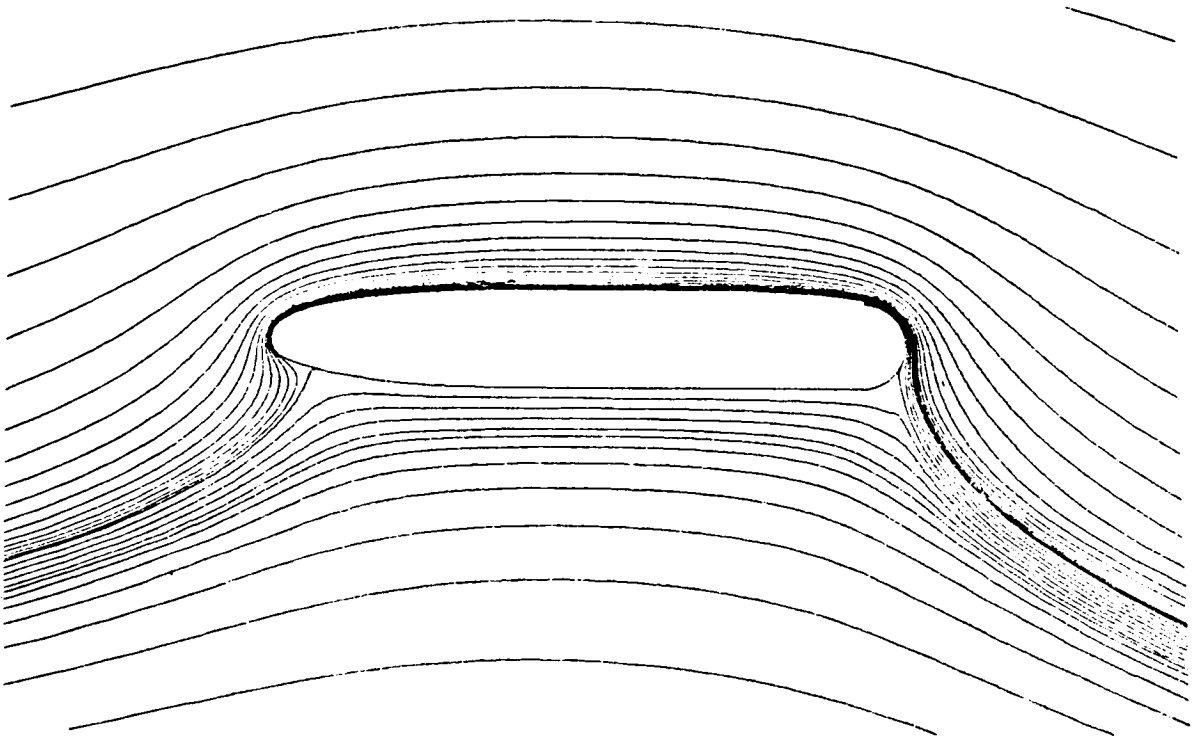

Figure 1. - Typical CCW Flowfield

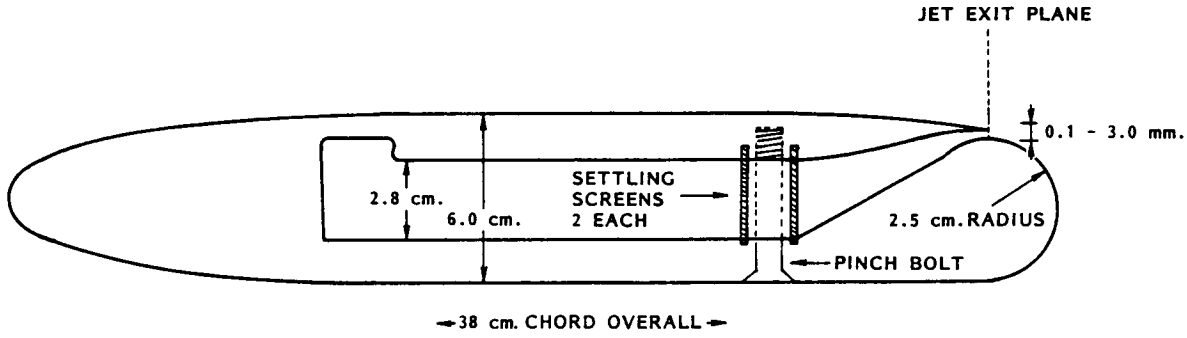

Figure 2. - CCW Model Construction

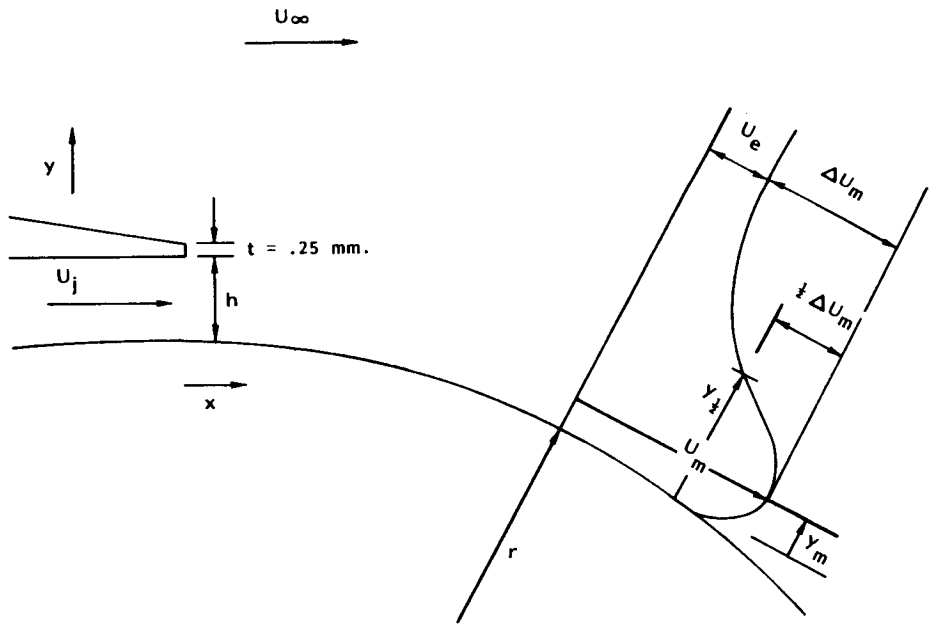

Figure 3. - CCW Slot Geometry and Nomenclature

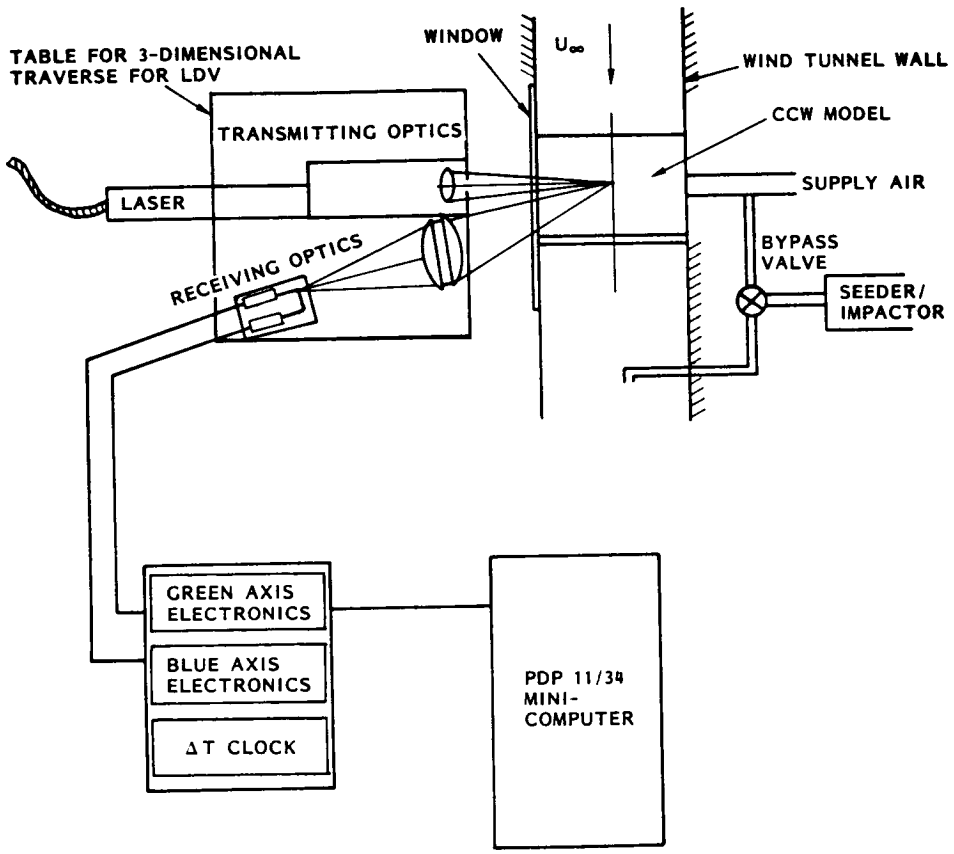

Figure 4. - 2-D LV Schematic

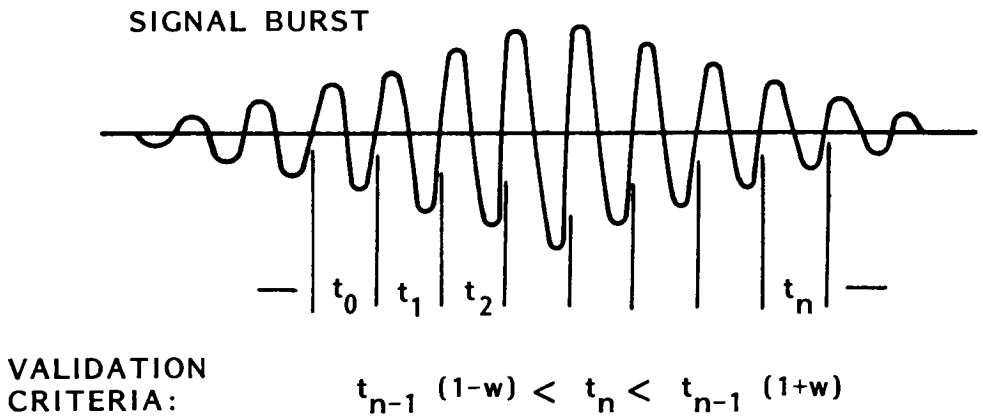

Figure 5. - Single Cycle Validation

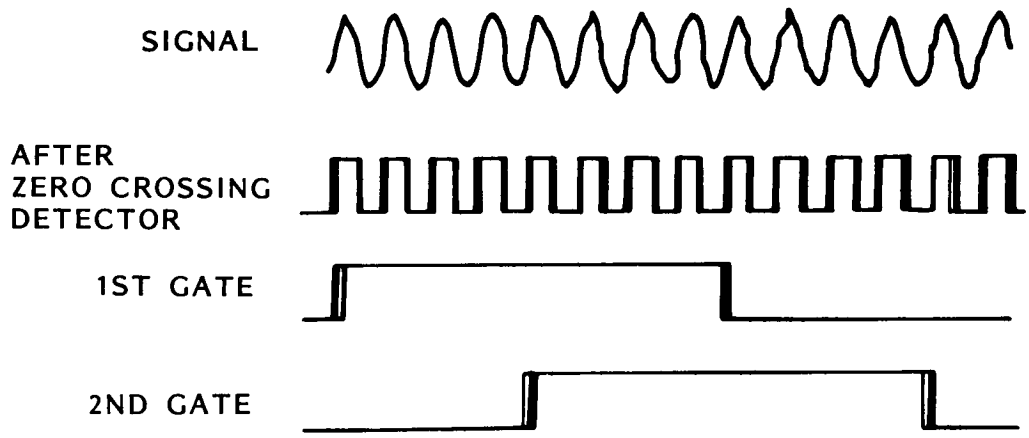

Figure 6. - Effect of Noise on Measurement Process

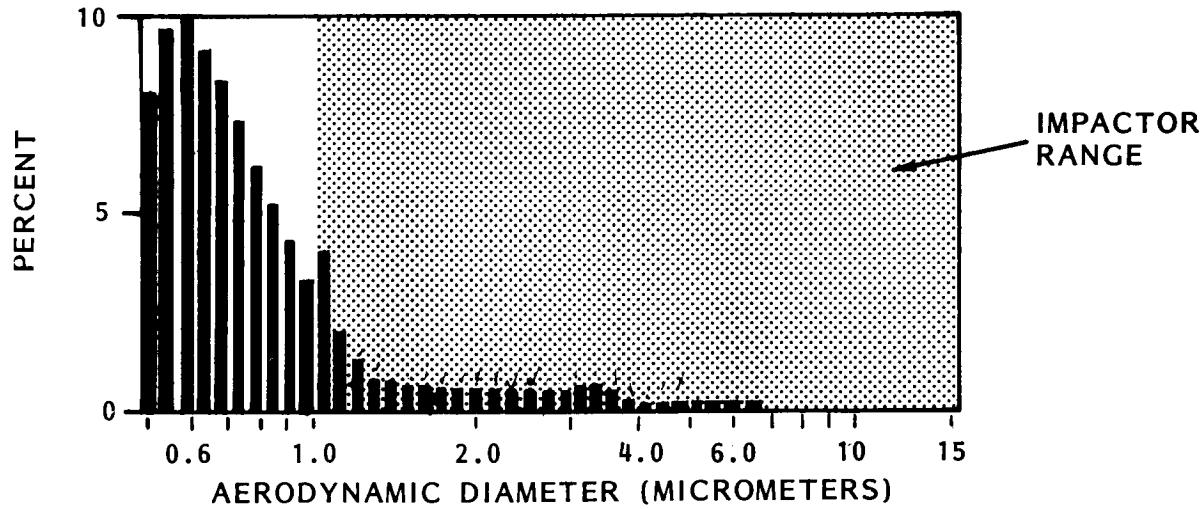

Figure 7. - Seed Size Distribution as Measured from Optical Particle Analyzer

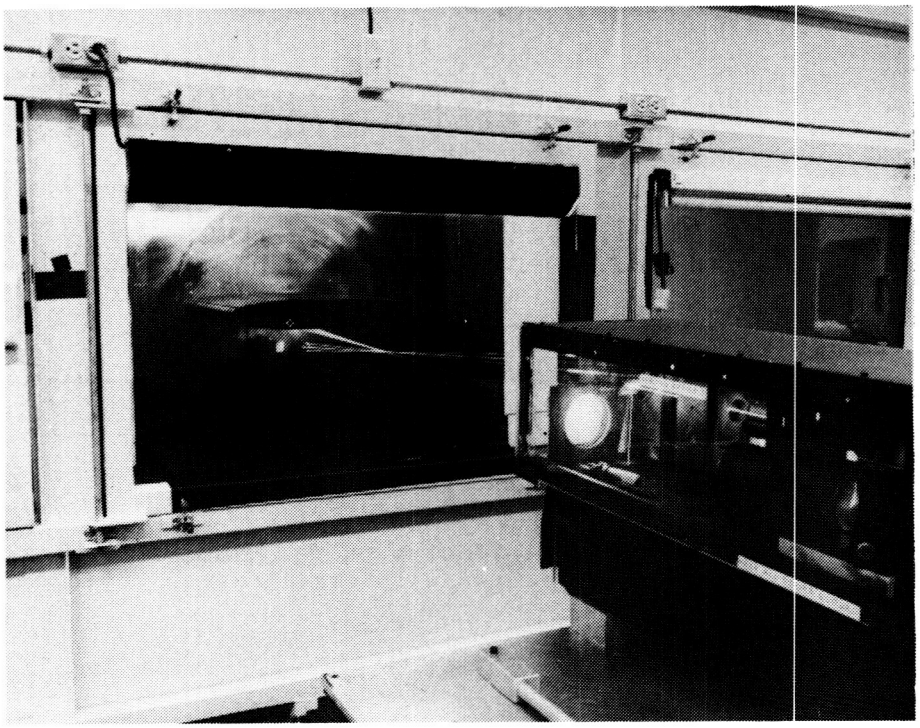

Figure 8. - CCW Model/Wing Tunnel Installation with LV Tranmitting Optics

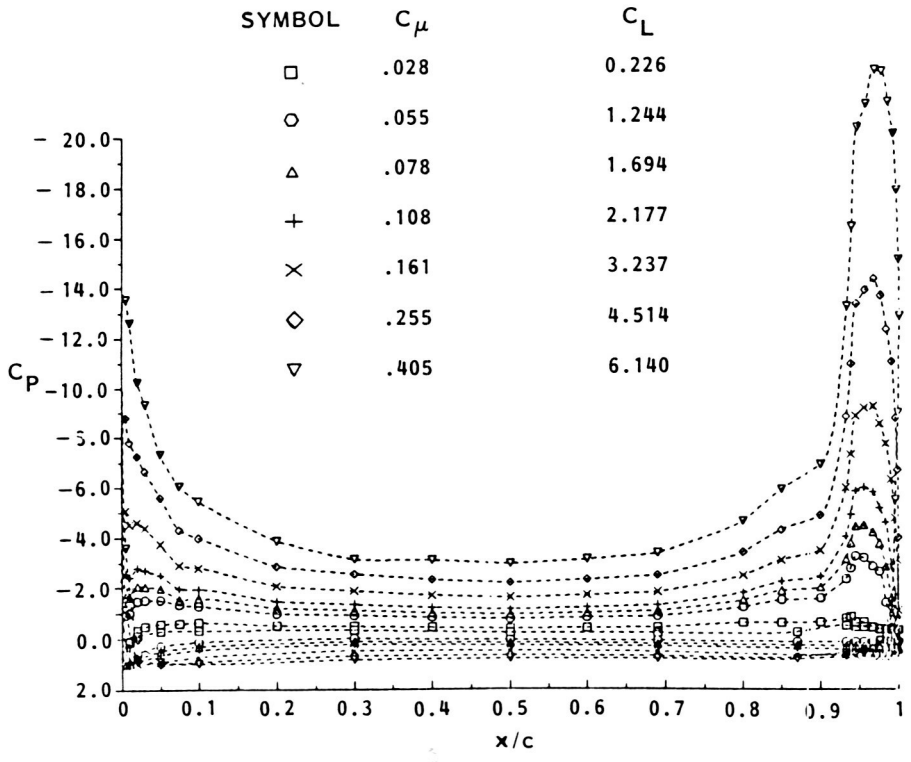

Figure 9a. - Surface Pressure Measurements at α =0.0 and h/r=0.10

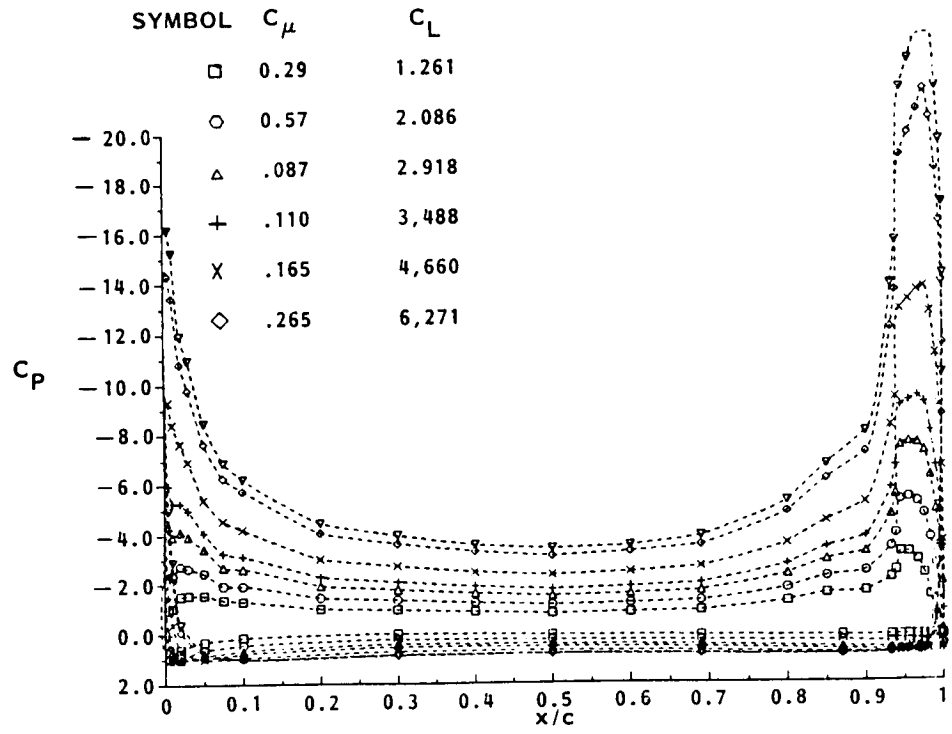

Figure 9b. - Surface Pressure Measurements at α =0.0 and h/r=0.034

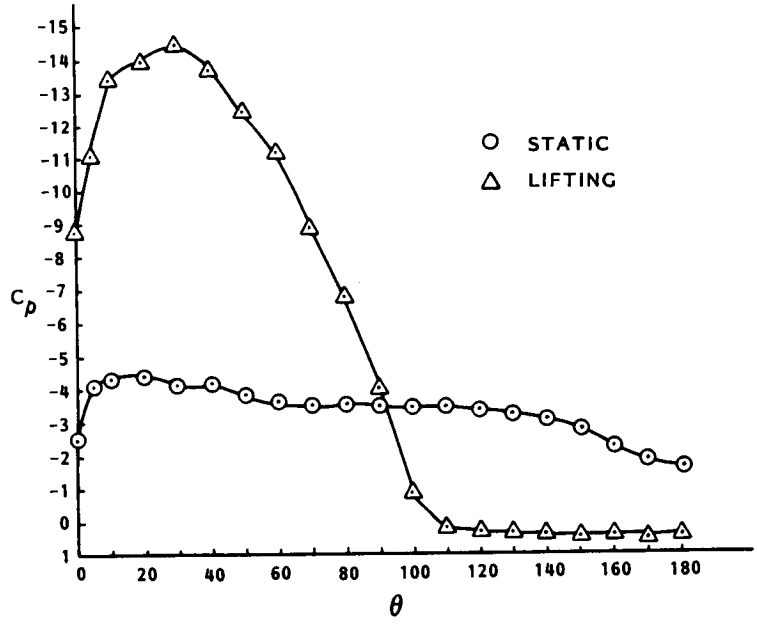

Figure 10. - Static Pressure Variation along the Coanda Surface

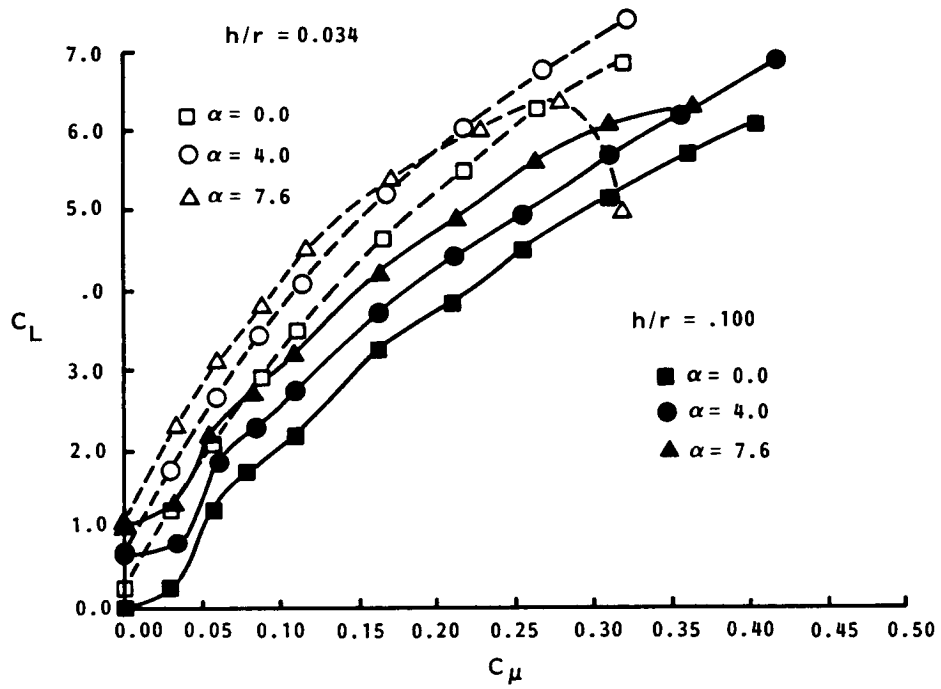

Figure 11. - Lift as a function of Jet Momentum and Angle of Attack

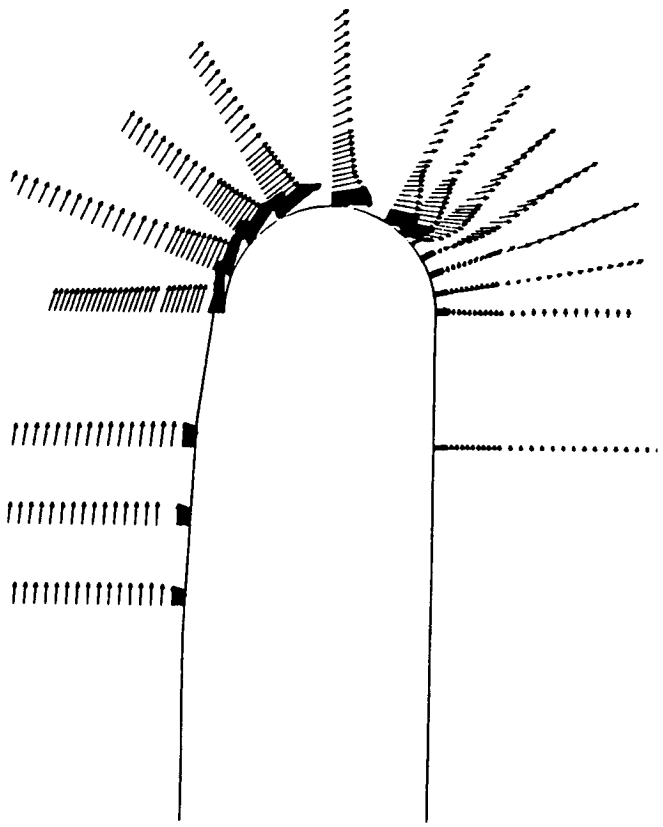

Figure 12. - CCW/LV Mean Velocity Vectors

C-2

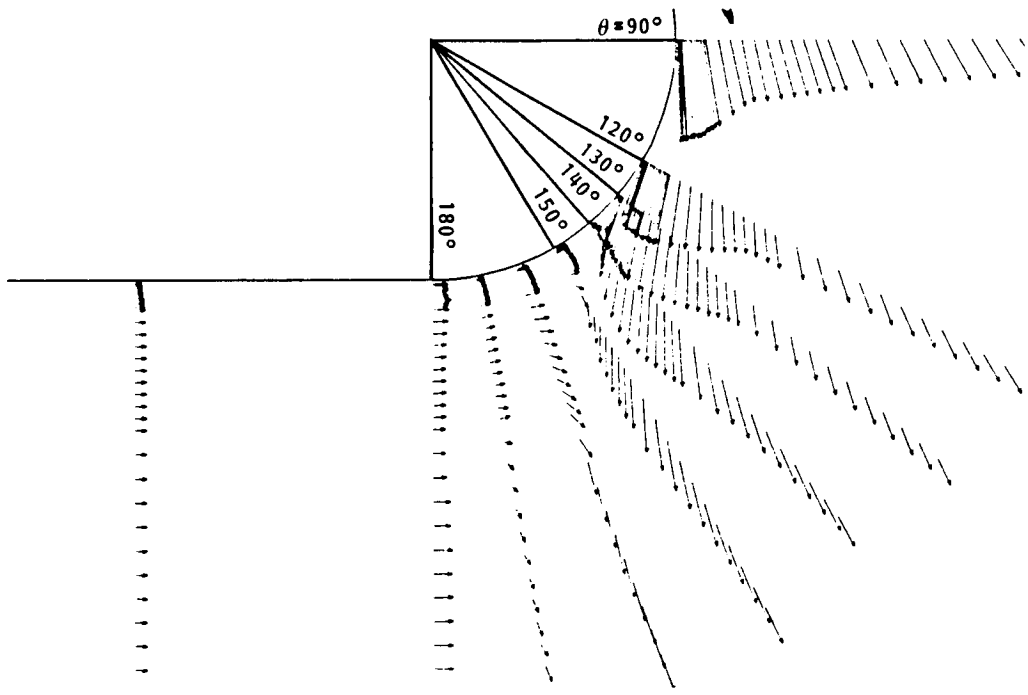

Figure 13. - CCW/LV Velocity Vectors in Aft-Stagnation Region

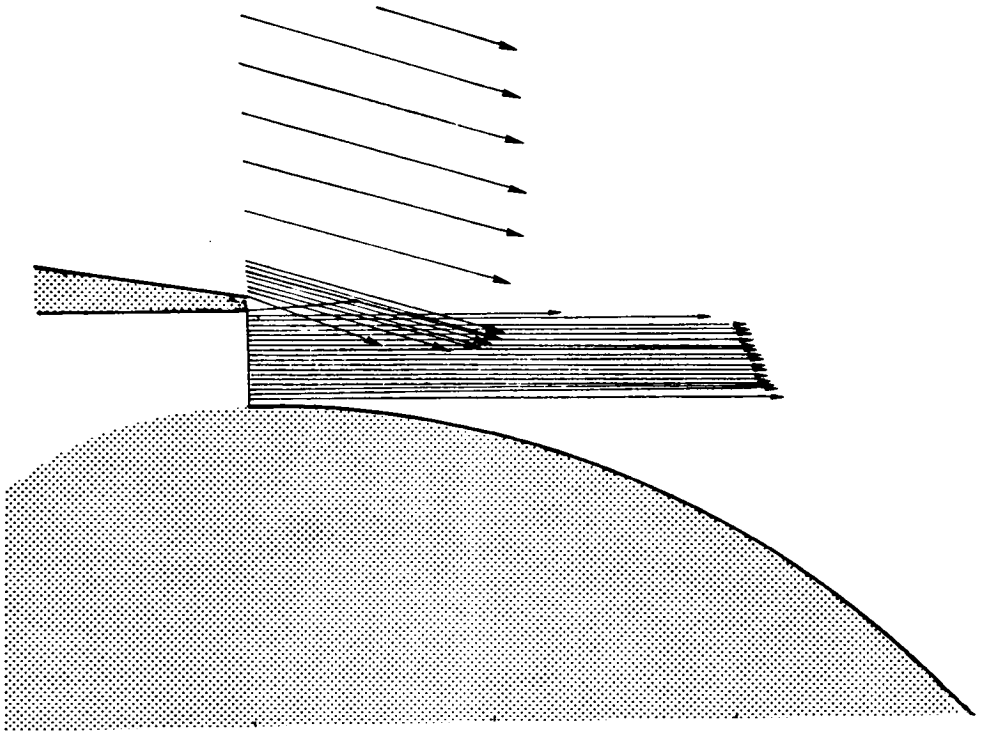

Figure 14. - CCW/LV Jet Exit Plane Velocity Vectors

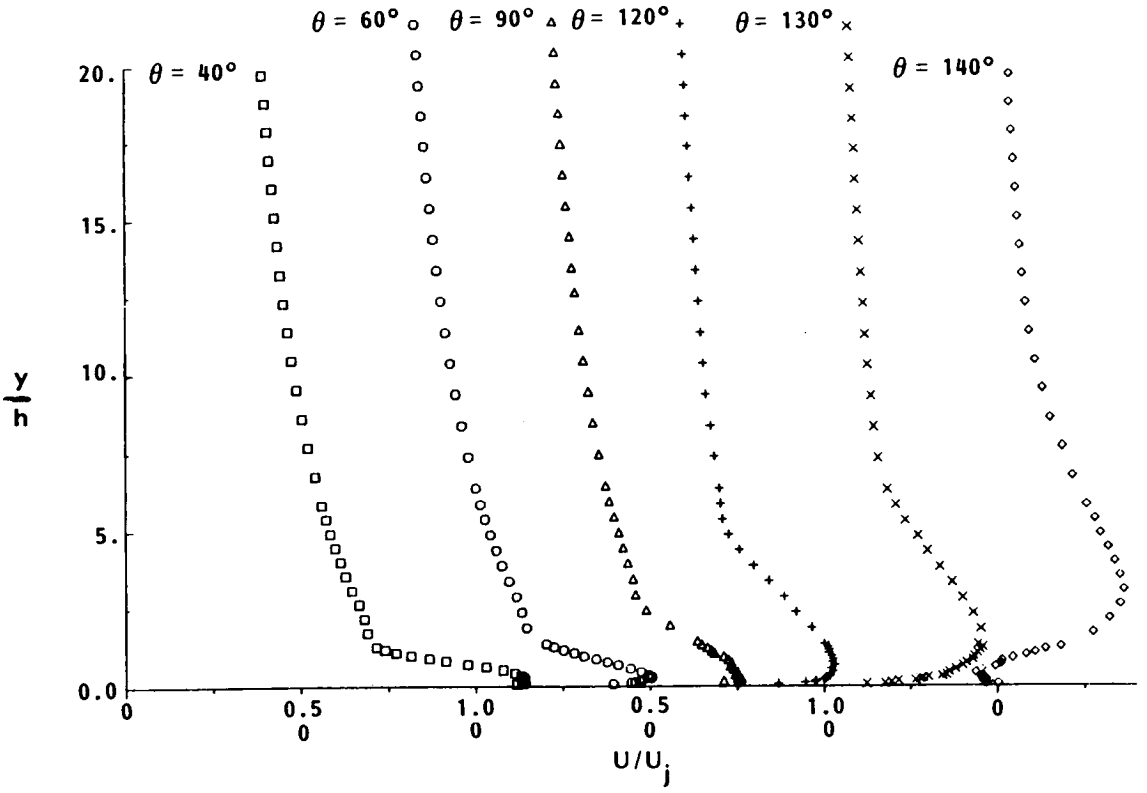

Figure 15. - Tangential Velocities in non-dimensional form

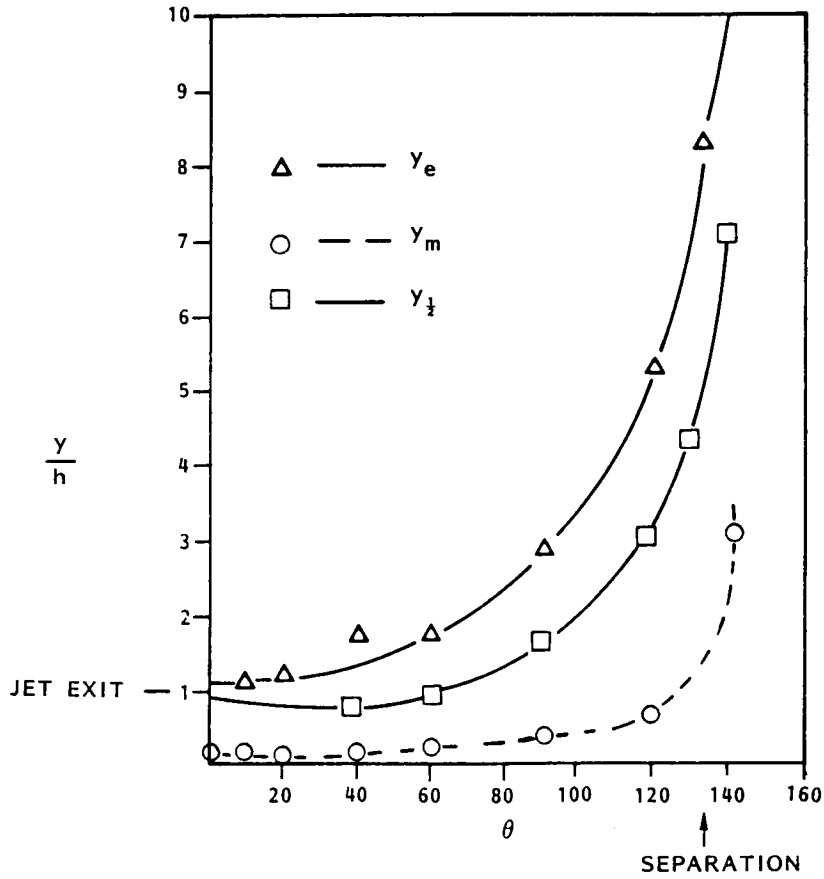

Figure 16. - Wall Jet Growth along Coanda Surface - Lifting case

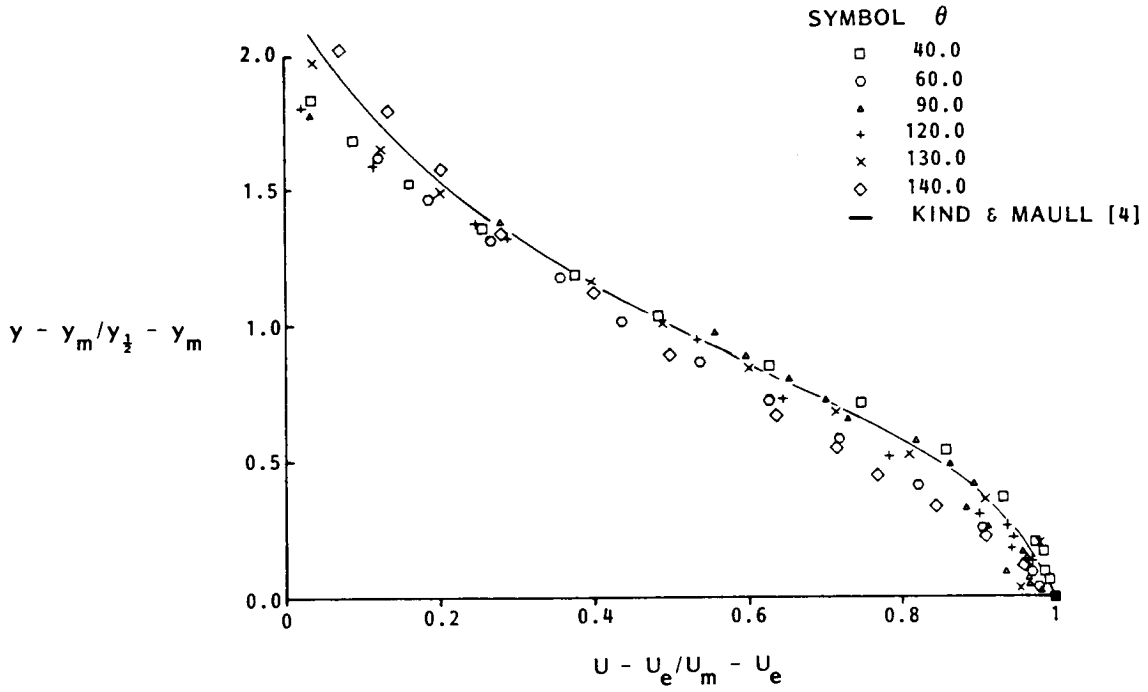

Figure 17. - Mean Tangential Velocity Profiles - Lifting case

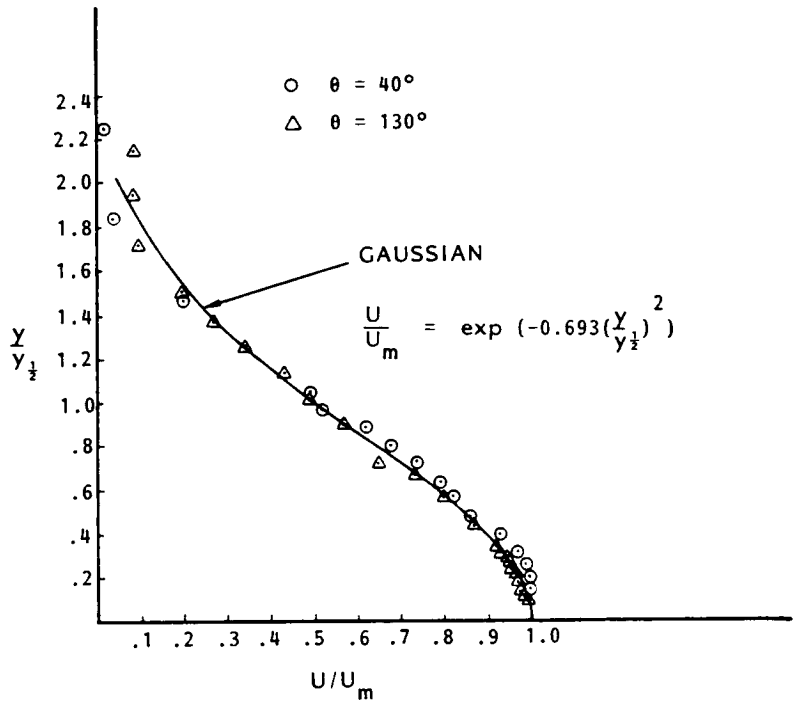

Figure 18. - Mean Tangential Velocity Profiles - Static conditions

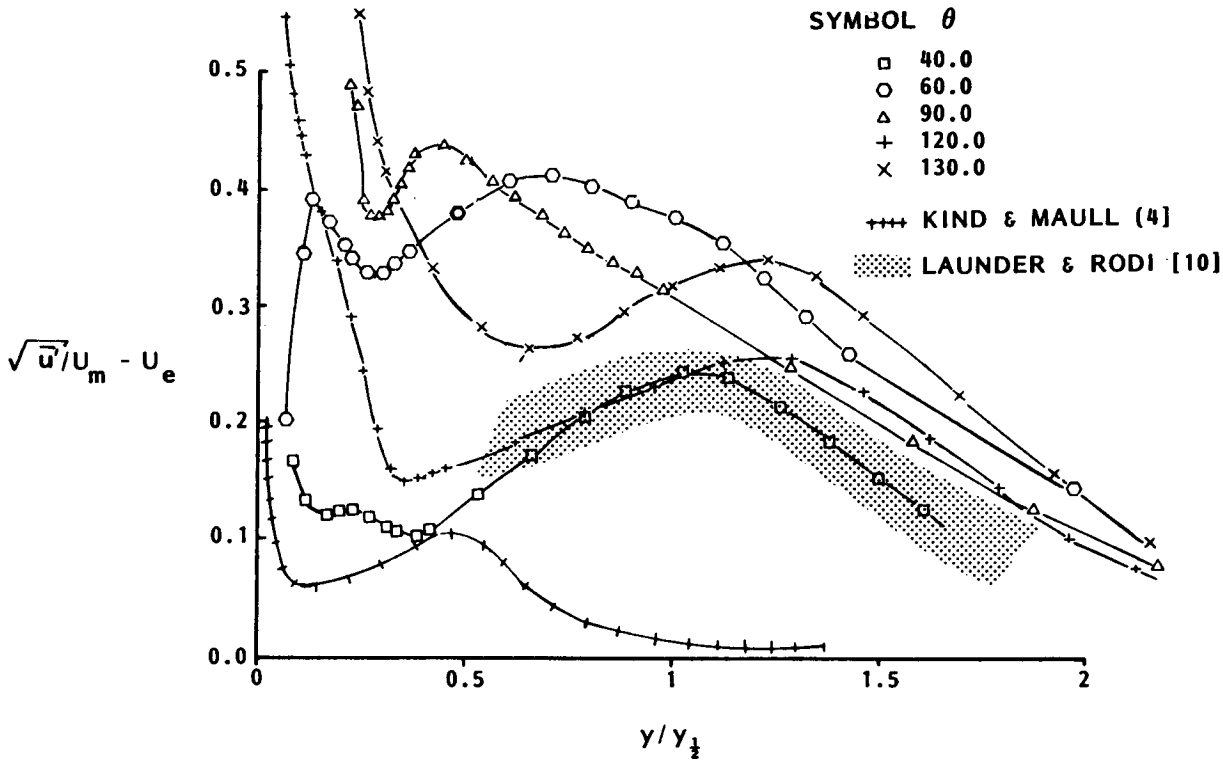

Figure 19. - Tangential Turbulence Intensity - Lifting case

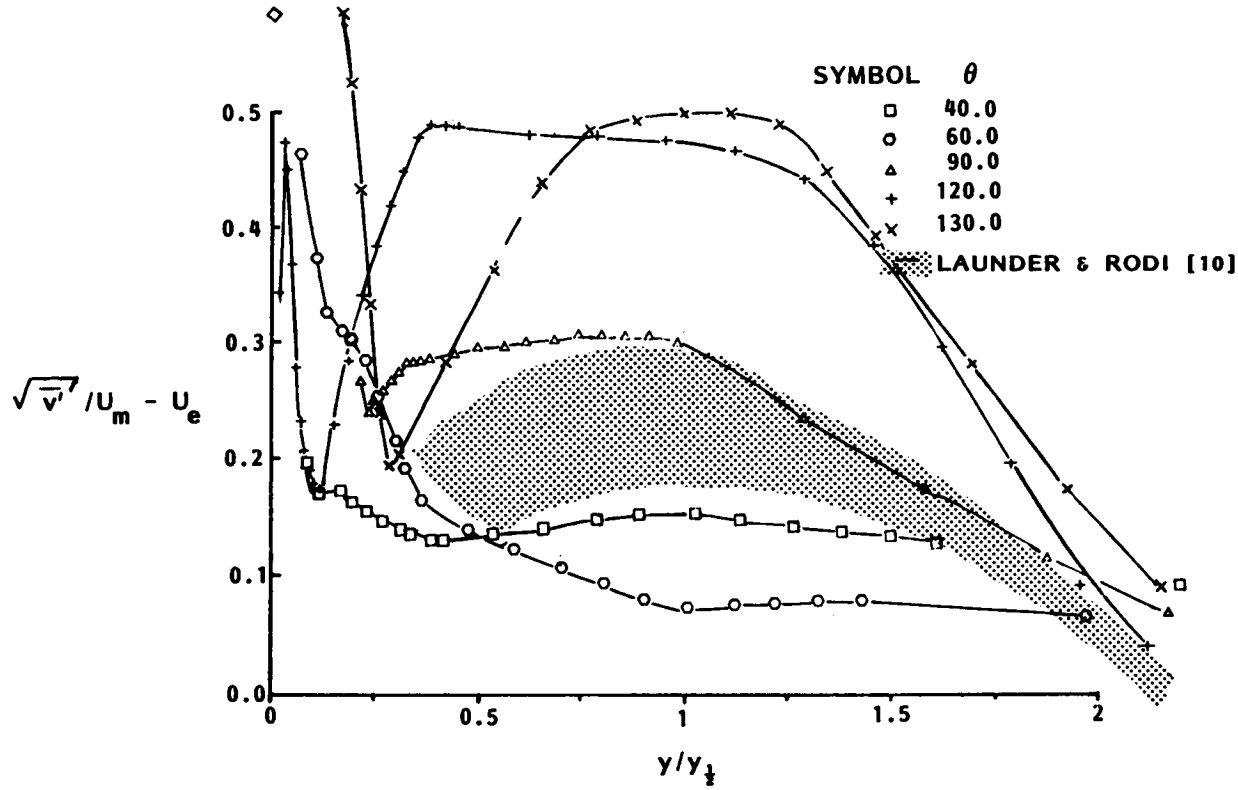

Figure 20. - Normal Turbulence Intensity - Lifting case

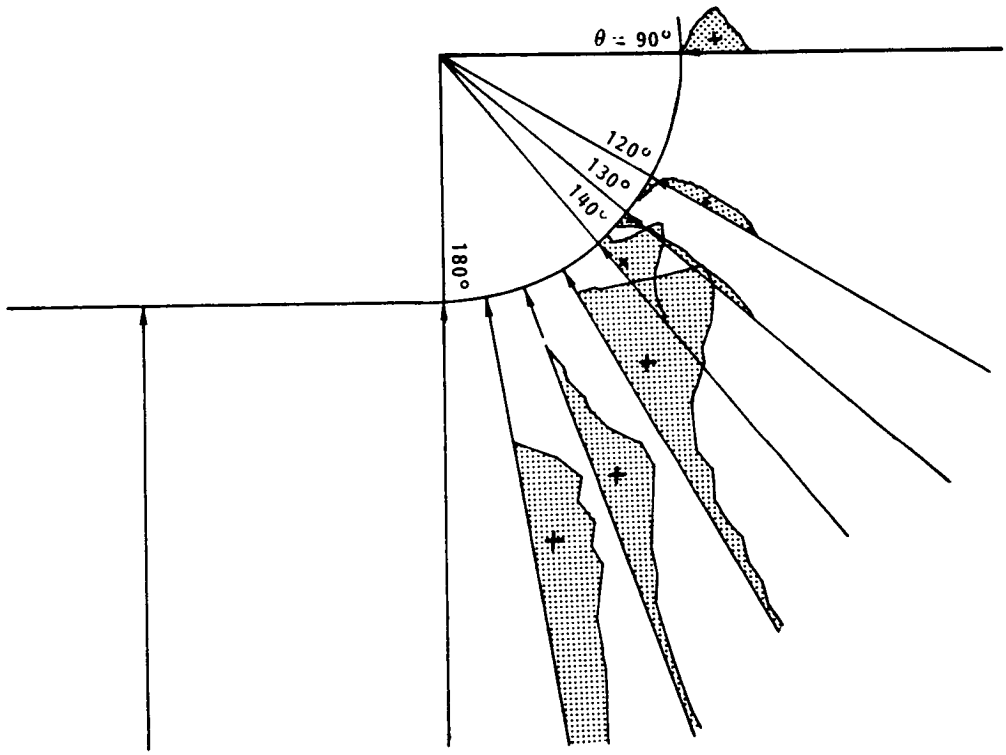

Figure 21. - Shear Stress Distributions in Aft-Stagnation Region - Lifting case

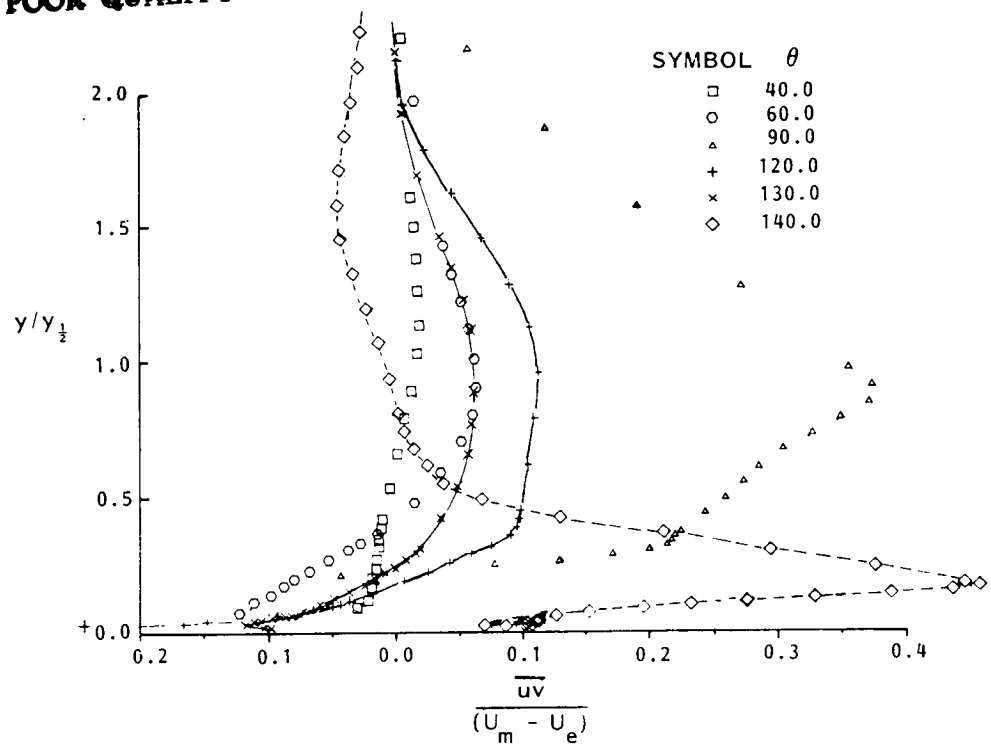

Figure 22. - Non-dimensional Shear Stresses - Lifting case

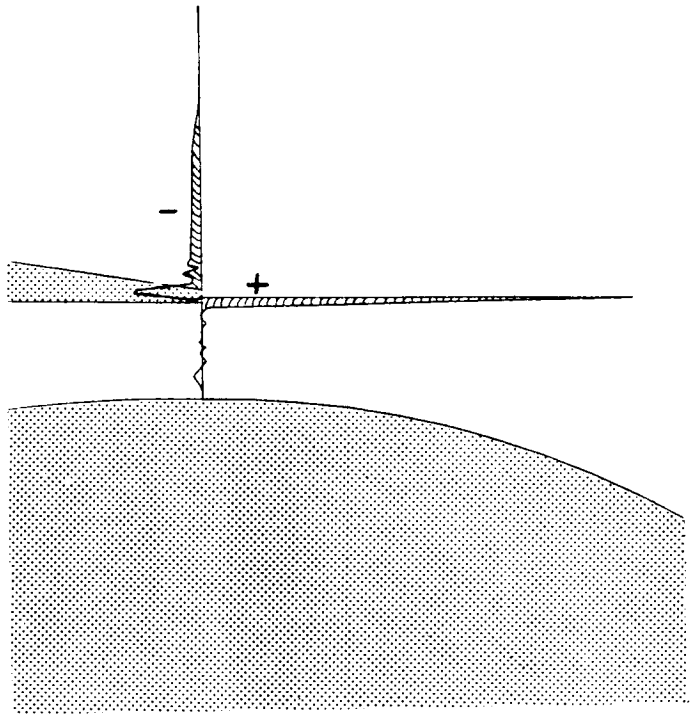

Figure 23. - Shear Stress Distribution in Jet Exit Plane - Lifting case

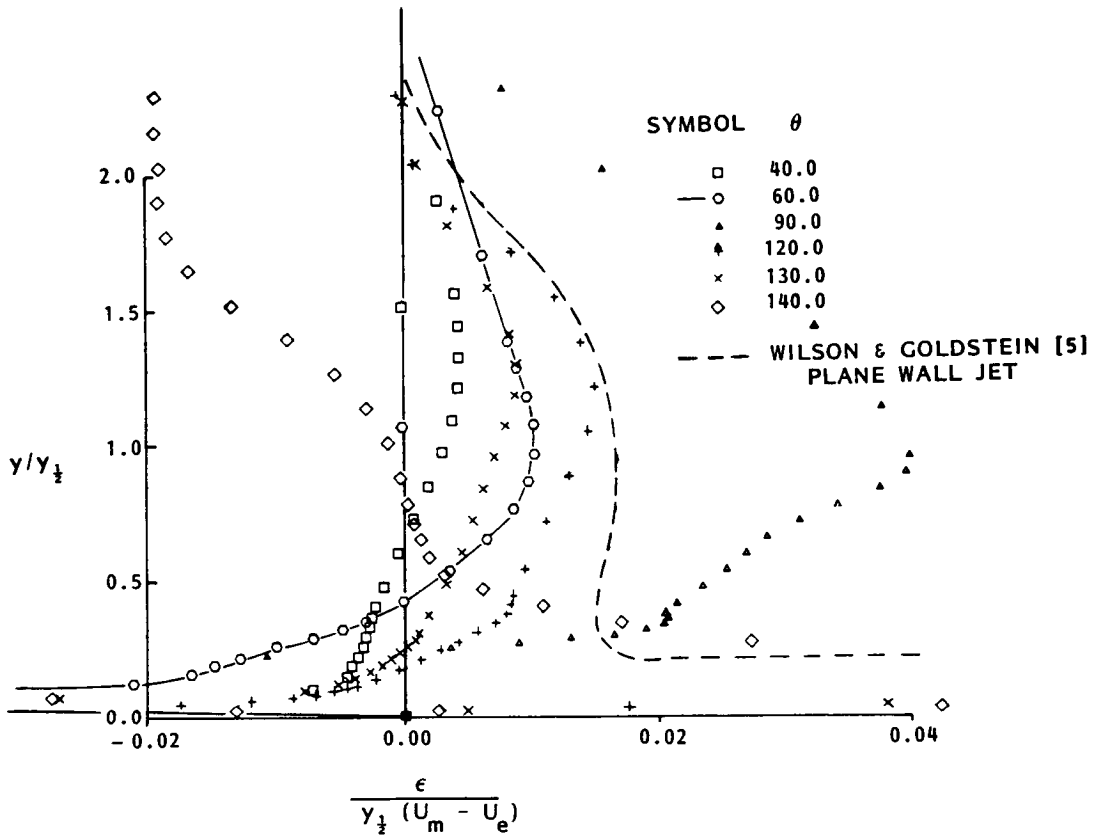

Figure 24. - Experimental Eddy Viscosities - Lifting case

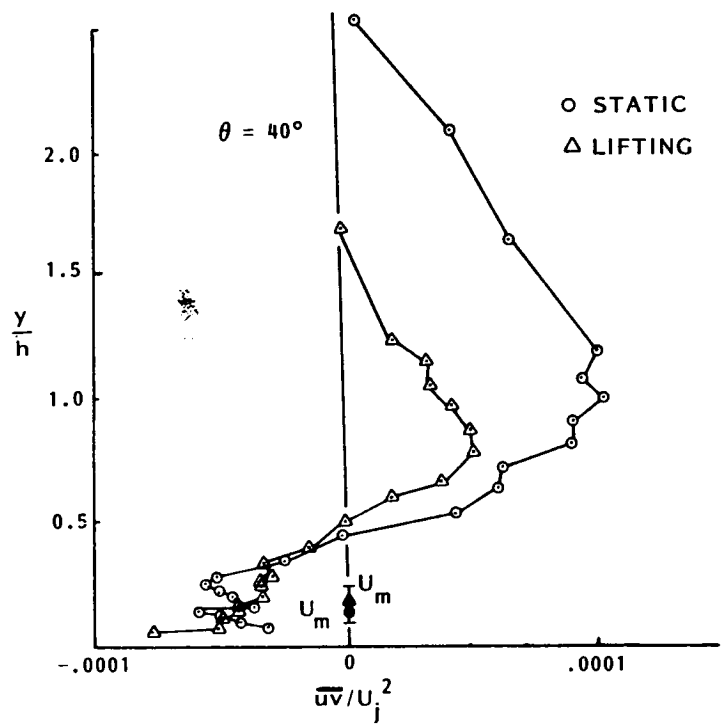

Figure 25a. - Near Wall Turbulent Shear Stresses, $\theta = 40^{o}$

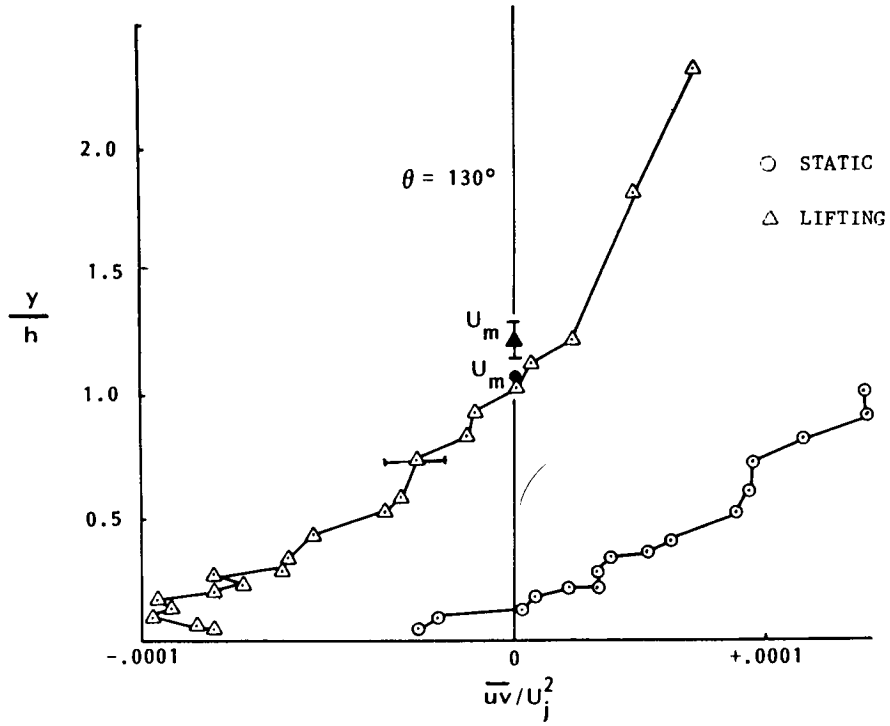

Figure 25b. - Near Wall Turbulent Shear Stresses, $\theta = 130^{o}$

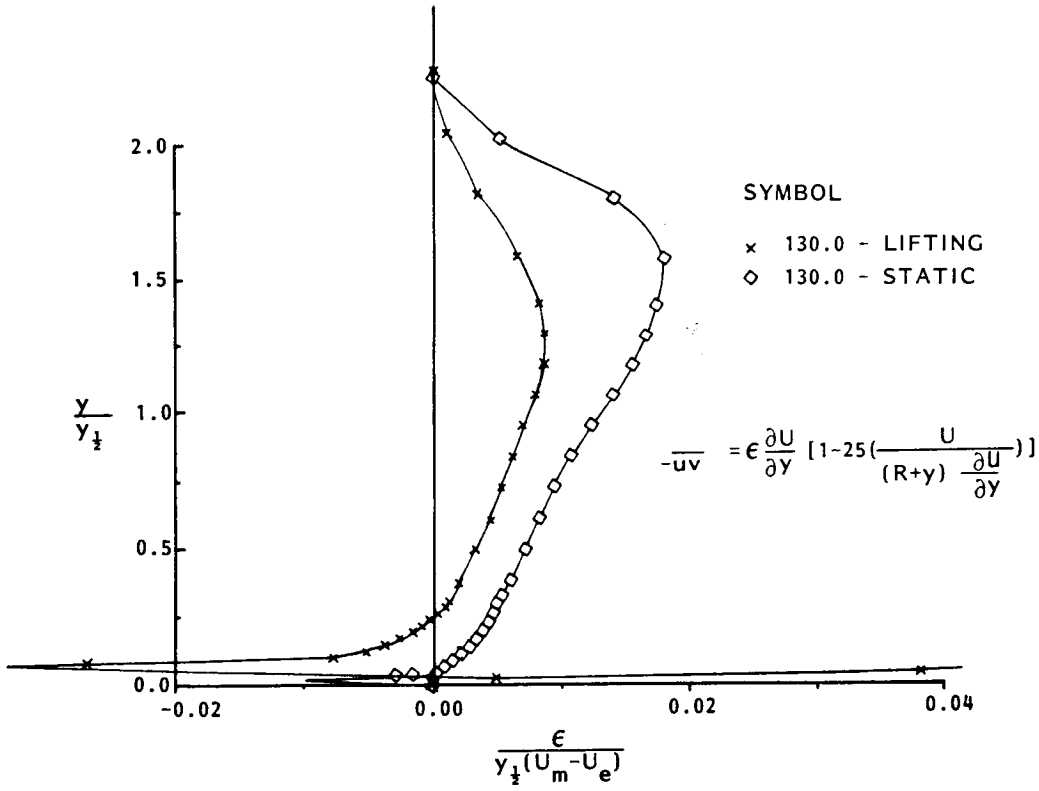

Figure 26. - Effect of Tunnel Freestream on Eddy Viscosities

	$U\frac{\partial U}{\partial x}$	$+\frac{UV}{R}$	$+(1+\frac{y}{R})V\frac{\partial U}{\partial y}$	$=$	$-\frac{1}{\rho}\frac{\partial(P+\rho\overline{v^2})}{\partial x}$	$-\frac{\partial}{\partial x}(\overline{u^2}-\overline{v^2})$	$-\frac{2\,\overline{uv}}{R}$	$-(1+\frac{y}{R})\frac{\partial\,\overline{uv}}{\partial y}$
LIFTING	$-O(10^0)+O(10^{-2})$		0	=	$-O(10^0)$	$+O(10^{-2})$	$-O(10^{-2})$	$-O(10^0)$
STATIC	$-O(10^0)+O(10^{-1})$		0	=	$-O(10^{-1})$	$-O(10^{-2})$	$-O(10^{-1})$	$-O(10^0)$

$\theta \doteq 90^0$

Figure 27. - Order of Magnitude Analysis at $\theta = 90^0$